FACTA UNIVERSITATIS
Series: **Mechanical Engineering**
https://doi.org/10.22190/FUME241230020B

Original scientific paper

A TOP-DOWN MULTISCALE ANALYSIS FOR DERIVING LOCAL MATERIAL PROPERTIES OF ADDITIVELY MANUFACTURED AL-SI ALLOY

Ruslan Balokhonov[1], Aleksandr Zemlianov[1], Artur Shugurov[1,3], Diana Gatiyatullina[1,2], Ivan Ivashov[1,3], Vasilii Balokhonov[1,2], Varvara Romanova[1]

[1]Institute of Strength Physics and Materials Science, SB RAS, Russia
[2]National Research Tomsk State University, Russia
[3]National Research Tomsk Polytechnic University, Russia

Abstract. *A Top-Down approach is proposed for the numerical-experimental determination of local material properties of an additively manufactured AlSi12 alloy possessing clearly expressed hierarchical structure. A thin-walled product was fabricated by wire electron beam additive technology. The alloy multiscale structure is studied experimentally by optical, scanning and transmission electron microscopy. The compression and nanoindentation mechanical tests are carried out. Based on the experimental data, the finite element models of a layered structure at the macrolevel, dendritic and composite cellular structures at the mesolevel, and a composite structure comprising an aluminum matrix and silicon particles at the microlevel are created. The proposed Top-Down analysis assumes sequential macro-meso-micro structure-based numerical simulations to derive the mechanical properties of aluminum in dendrites at the microlevel and aluminum in the eutectic at the submicron level. The stress concentration and the plastic strain localization in dendritic, cellular and composite structures are analyzed. It was found at the mesoscale that the eutectic material experiences more shear stresses than the aluminum dendrites, with the highest stresses being observed in between the closely located dendrites. The volumetrically tensile and pure shear regions, as well as the regions of low elastic strains, are found after 30% compression.*

Key words: *Multiscale analysis, Additive manufacturing, Aluminum-silicon alloys, Microstructure-based numerical simulation, Plastic deformation*

Received: December 23, 2024 / Accepted May 30, 2025
Corresponding author: Ruslan Balokhonov
Institute of Strength Physics and Materials Science SB RAS 634055, Tomsk, pr. Akademicheskii, 2/4, Russia
E-mail: rusy@ispms.ru

1. INTRODUCTION

The design of multiscale models adequately describing deformation and fracture of newly developed advanced materials has been a continuing challenge for mechanics and materials science. It is primarily necessary to develop and study such models as applied to composite materials demonstrating pronounced structural inhomogeneity. It is the complex hierarchical structure of composites which makes their behavior hardly predictable in the frame of single-scale approaches. The stresses may concentrate at the interfaces between the structure components and the plastic flow can localize in their vicinity, which would affect the macroscopic material response and result in a premature loss of the strength. A number of present-day studies in the field of multiscale modeling have been thoroughly reviewed [1]. The authors discuss the analytical, semi-analytical and numerical methods for modeling composites and analyzing their effective properties. There are two major approaches in the multiscale numerical modeling: bottom-up and top-down. The former assumes the solution of a series of direct problems on structure deformation at different scale levels (e.g. micro-, meso-, and macroscales), starting from the lowest level. The effective material properties are determined at every level via homogenization and then used at higher levels as the model parameters. Note that this approach assumes the material properties at the lowest level to be known in advance: they are frequently selected from the data of macroscopic experiments or estimated from indirect experiments. However it is the derivation of the local material properties, presumably differing at different scales, which is the most acute problem of multiscale approaches. It has been noted [1] that the finer the scale, the more difficult it is to experimentally verify the material constants in the model and to measure the properties of microstructure inhomogeneities. There are some recent examples of an implementation of the bottom-up approach [2, 3]. In a two-level modeling scenario [2], the authors introduced the strain rate and the matrix and fiber properties at the microlevel aiming at determining the fiber characteristics at the mesolevel, where the dynamic properties of braided composites are predicted. The purpose of a multiscale approach [3] is to identify the effect of porosity on mechanical properties and damage mechanisms of multidirectional carbon-fiber-reinforced polymer (CFRP) composites. The data on the direct finite-element modeling of CFRP composites with varying pore volume fractions and pore sizes are used for a stochastic multiscale prediction of mechanical response of the laminates. The principal task of a top-down approach is the solution of an inverse problem of determining the local material properties at the lower scales using the data of macroscopic and other special experiments. The bottom-up and top-down approaches can be combined to provide an iterative determination and refinement of the local material characteristics [1, 4], while multi-criteria decision-making framework can be used in composite material selection by comprehensive sensitivity analysis methods [5].

Additively manufactured composites represent a class of advanced materials for which the issues a multiscale analysis are most important. This is due to the fact that a natural structural inhomogeneity of the composites, manufactured using conventional processes and associated with the availability of heterogeneous materials (particles, fibers, and matrix) in them, is added with the morphological and crystallographic anisotropy related to the manufacturing method – 3D printing. Due to multiple thermal cycling and high temperature gradients in the additive manufacturing, a complex, hierarchically organized structure is formed, which contains melt pools and interlayers between the deposited layers, as well as a specific structure within the melt pools and at the boundaries in between. There

are two most versatile additive-manufacture processes: powder bed fusion (PBF) and directed energy deposition (DED). In the former case, the components are manufactured by a preliminary deposition of thin powder layers on a platform and their compaction with a roller, followed by the layer-by-layer laser (L) or electron beam (E) fusion [6]. In the E-PBF, the powder is preheated and the particles fuse in vacuum [7, 8]. The L-PFD process, also referred to as selective laser melting (SLM), uses a high-power laser to melt the powders in an inert atmosphere without any pre-heating. Similar to 3D-printing polymeric materials [9], the metallic materials used in the DED process are either powders or wires fed through a nozzle, which are melted by a laser, an electric arc, or an electron beam. The DED method is perfect for repairing high-cost components with a negligible material loss [10]. The resulting material structure and texture heavily depend on the additive manufacturing process and its modes. For instance, the particle size or wire diameter in DED are relatively large compared to those in PBF, which results in a larger melt pool or layer and interlayer thickness. By giving preference to E-PBF instead of SLM, one can increase the alloy hardness and ductility due to structure refinement and second-phase precipitation prevailingly at the grain boundaries [11]. A repeated high-energy electron-beam irradiation of the material surface can improve the strength of a sample fabricated by the wire-arc additive manufacturing (WAAM) technology [12]. The spatial grain-size distribution, inhomogeneous in three dimensions, might strongly depend on the E-DED strategy, and an additional annealing treatment can increase the texture strength and structure homogenization [13]. The resulting E-DED alloy structure can be affected by the thickness and material properties of the substrate [14] and the final sample shape: whether it is a thin-walled product or a bulk item [15]. Furthermore, the beam power and the wire feed and displacement rates can significantly influence the final product shape and quality [16].

Aluminum alloys and composites thereof have been extensively used in the aerospace industry due to their high energy efficiency [17] and are, therefore, frequently applied in additive manufacturing. The latest advances in this field have been overviewed, for instance, in [18], where the authors provided a detailed description of the structure formation and mechanical properties of aluminum alloys, Al-Si among them, and aluminum-matrix composites manufactured using a variety of AM processes. In the wire-feed additive manufacturing, the energy of a laser is frequently used. In a different study [19], a hot Al-Si6 wire was deposited on an Al6061-T6 substrate. Using the method of digital image correlation (DIC), the authors demonstrated that in the samples in tension the deformation localizes in the near-boundary regions of the melt pool, which results in a characteristic serration of the stress-strain curve. This is due to the fact that primary aluminum dendrites in the regions adjacent to the melt pool boundaries are coarser than those in the material bulk. The WAAM technology is currently becoming increasingly popular. The size effect of ceramic powder particles, added between the layers of Al-Si6 alloy, on the fusion process and material microstructure was studied elsewhere [20]. The authors demonstrated that a coating WAAM-manufactured from nanosized powder allows significantly decreasing the arc fluctuation and provides its correct deflection, which improves the molten pool fluidity and the forming quality. An interlayer coating can favor a grain size decrease and a transition from columnar crystals to fine equiaxed dendrites, which improves the rupture strength of Al-Si6 alloy both along and across the printing direction. A combined laser-arc technology for manufacturing Al-Si12 alloy was proposed in [21]. It is shown that high-frequency circular vibrations of a laser beam improve the

forming precision, decrease the structure element size, and increase the yield strength and relative elongation of the alloy. The use of an electron-beam energy impact in wire- and powder-feed additive manufacturing of alloys and composites, Al-Si among them, has been described in a recent review [22]. The authors analyzed the features of defect structure formation in dependence of manufacturing modes, wire and powder states, scanning strategy, and conditions of additional ultrasonic processing, laser treatment or shot peening. The wire-feed electron-beam additive manufacturing (WEBAM) demonstrates clear advantages over the laser additive process, since it occurs under the vacuum conditions, which allows preventing oxidation of aluminum alloys, and the energy density and the heat penetration depth are much higher than those of the laser technology [23, 24].

Earlier we performed a multiscale analysis of deformation and fracture in an *aluminum matrix – carbide particle* composite material [25] and used a bottom-up approach in a numerical study of deformation of a WEBAM eutectic Al-Si12 alloy [26–28]. We demonstrated that this alloy is a multiscale composite material. At the submicron scale, its eutectic network contains disperse silicon particles measuring hundreds of nanometers, which are surrounded by an aluminum matrix. The peculiarities of formation of residual stresses during cooling of this composite and its subsequent mechanical loading were investigated using the literature data on the properties of aluminum and silicon [26]. At a higher scale level of tens of microns we revealed the formation of a dendritic structure. A two-level approach is illustrated elsewhere [27], wherein the effective eutectic network properties were determined via homogenization of the solutions to the problem of deformation of a silicon particles–aluminum matrix composite at the submicron level. When solving a series of direct problems, we studied the influence of mechanical properties of the aluminum matrix on the composite structure strength. More recently [28], the two-level approach was applied in the investigation of the effect of an interlayer on the deformation and fracture of dendritic structures. In so doing, the properties of aluminum at the submicron and micron levels were determined using indirect experimental data on the grain-size dependence of its yield stress and strength.

The purpose of the present study is to apply a top-down approach to determining the plastic properties of aluminum at the micro and submicron levels, relying on the data of nanoindentation macroscopic experiments.

2. Additive Manufacturing and Microstructure Analysis of Al-Si12 Alloy

The samples were printed using a wire-feed electron-beam additive manufacturing technology in a laboratory setup designed at the Institute of Strength Physics and Materials Science SB RAS (Tomsk, Russia). Its operating principle is the following: an electron gun generates an electron beam to form a stable melt pool. To this aim, a larger beam sweep diameter is selected than that of the wire. Therefore, part of the beam heats and melts the upper substrate layer and the other part heats and melts the wire. The resulting liquid metal via the jet or drop transfer is fed into the liquid metal pool formed in the substrate. In order to form directed layers, use is made of a three-coordinate, water-cooled table. During printing, the beam is not shifted, only the table is displaced at the controlled velocity and direction. The electron beam parameters (current and accelerating voltage) can be regulated during printing, which, together with the regulation of the table motion and wire-feed, provides a flexible control over the printing modes. The manufacturing process is carried out in vacuum.

In this study we printed a thin-walled sample with a length of 8 cm, a single layer thickness of 5 mm and a height of 3 cm [27]. A eutectic AlSi12 alloy ESAB OK Autrod 4047 1.2 mm wire was deposited layer-by-layer onto a AlMg5 alloy substrate, using an optimal deposition mode with an exponentially decreased energy input to compensate for the fast cooling of the first layers from the substrate. This allowed forming the samples with minimal defects of porosity and discontinuities and prevented spreading of the top layers [27]. Fig. 1a shows the sample section.

We examined the EBAM product structure using metallography and scanning and transmission electron microscopy. The metallographic studies were performed according to a standard procedure. The samples measuring 10x10 mm were cut from the middle part of the product, ground on an abrasive paper of 200 to 2000 grits, and polished using a diamond paste and a suspension. The surfaces of the metallographic sections were examined in an Olympus LEXT OLS4100 microscope. The sample microstructure was studied in a TESCAN VEGA II LMU scanning electron microscope (SEM) and in a LEO EVO-50 microscope equipped with a system for the energy dispersive microanalysis (EDS). Thin foils for the TEM studies in a JEM-2100 transmission electron microscope (Tokyo Boeki Ltd., Japan) were prepared by mechanical grinding on abrasive paper and ion thinning in an EM-09100IS ion slicer.

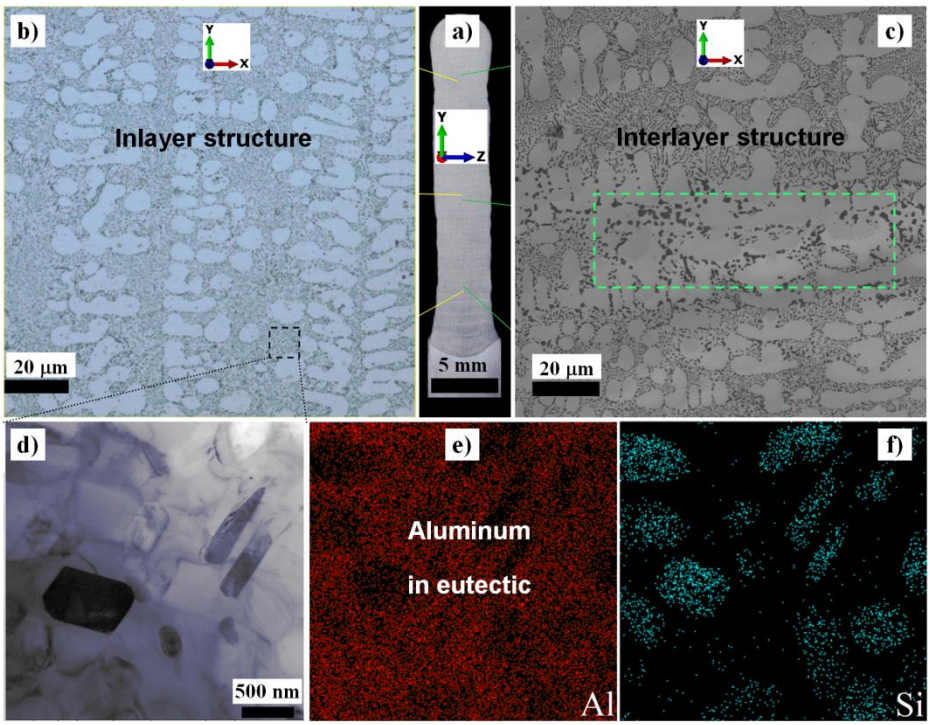

Fig. 1 Multiscale nature of WEBAM AlSi12 alloy. Optical images of the thin-walled printed sample cross section (a), inlayer dendritic structure (b) and interlayer cellular structure (c). Bright-field TEM image of the eutectic Al-Si composite (d) and corresponding EDS maps showing distribution of Al (e) and Si (f)

The microstructural investigations have demonstrated that the additively manufactured AlSi12 alloy has a complex multiscale structure and represents a multiscale additive composite. As compared to conventionally manufactured AlSi12 alloys there are the following specific features unique to the WEBAM alloys. At the macrolevel, this thin-walled sample represents a layered product in which the fused layers alternate with interlayers – direct sites of fusion in the heat affected zone (HAZ) (Fig. 1a). The material structure in the printed layer and at the fusion interface is different (cf. Fig. 1b and c). In the former case, we observe coarse aluminum dendrites of a few tens of microns, which are surrounded by a eutectic network. The eutectic network, in its turn, was revealed by the TEM examination as the volumetric silicon particles of hundreds of nanometers having different shapes, which are surrounded by the aluminum matrix (Fig. 1d–f). The interlayer structure is absolutely different. Between the layers in the zone affected by the electron beam there is a 30–50 μm thick interlayer formed from the fused aluminum containing agglomerated silicon particles (Fig. 1c). These particles have more complicated shapes and an order of magnitude larger size than the submicron particles in the eutectics; they are distributed over the volume as a cellular structure.

3. MULTISCALE NUMERICAL MODELING PROBLEM FORMULATION

3.1 Model Structures of Different Spatial Scales

Using the experimental images given in Fig. 1, four geometrical models were designed at every spatial scale level. A model of the layered structure of a macrosample, wherein the printed layers alternate with thin interlayers at the layer fusion boundary, is presented in Fig. 2a. The dimensions of the model macrosample correspond to those of the experimental sample subjected to uniaxial compression in the scanning direction. According to the experimental data (Fig. 1a), the average printed layer thickness is on the order of 400 μm, with an interlayer of an average thickness of 50 μm observed between the layers (Fig. 1c). Thus, the volume fraction of the printed layer and the interlayer is about 89% (Fig. 2b) and 11% (Fig. 2c), respectively. We included a fourth part of the sample into our calculations; the symmetry conditions were set on the right and back surfaces. To sum up, the geometrical model of this macrosample contains 6 layers and 6 interlayers. The number of finite elements in the layered structure is about 2 million.

The model structures at the meso- and microlevels (Fig. 2d–f) were designed based on the following considerations. We take that the structures at the mesolevel are representative. Therefore, the total volume fractions of aluminum and silicon have to be 86% and 14%, respectively, i.e. equal to their percentages in the initial feed wire for printing. In the experiment, the volume fraction of aluminum dendrites after additive printing is found to be 42 %, and that of the eutectics – 58 %. The same ratio was used at the mesolevel when designing the model dendritic structure whose morphology (Fig. 2d) corresponds to the experimentally observed morphology (Fig. 1b). The size of the designed structure is on the order of 100×120 μm, and it is digitized by a regular rectangular mesh of 500×600 elements. Since at the microlevel the eutectic material contains the entire 14 % of silicon, the volume fraction of silicon in the model composite eutectic material would be 24% (Fig. 2f). The numerical model of the Al-Si composite structure has the size of about 2.5×2.5 μm; the computational domain contains 230400 finite elements. The size of

the cellular structure in the interlayer at the mesolevel (Fig. 2e) is 100×30 μm and the computational domain size is 720×250 elements. The volume fraction of silicon particles is 14 %; when the next layer is printed, the material in the heat affected zone is remelted, and silicon particles contained in the eutectics agglomerate to form coarser particles surrounded by the aluminum inherited from the eutectics and the dendrites.

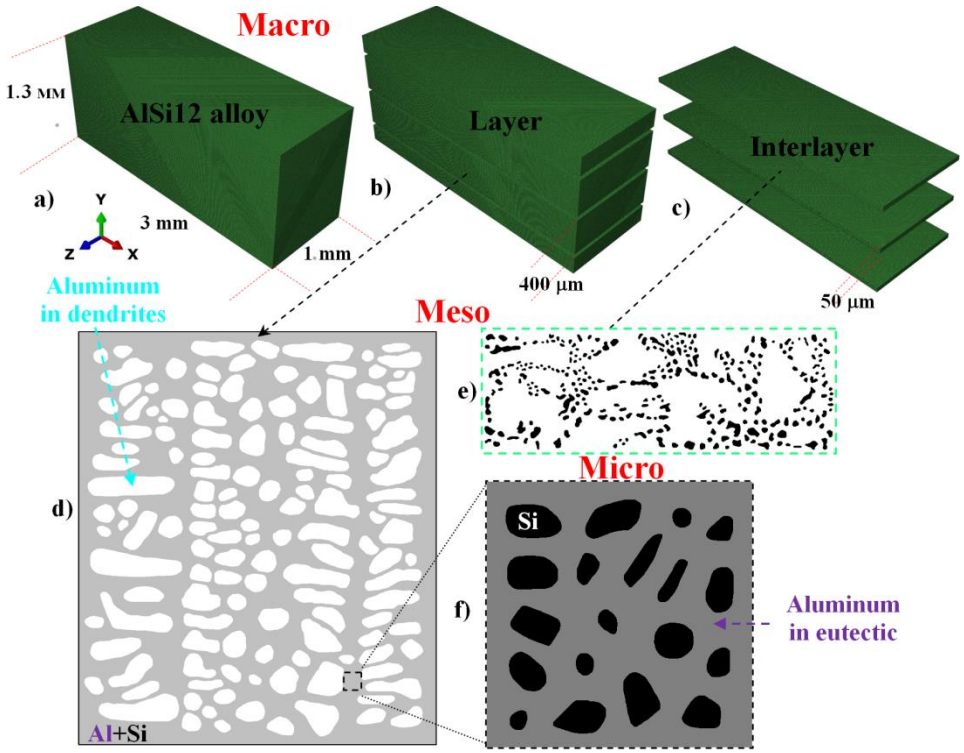

Fig. 2 Layered macrosample cut from thin wall (a–c), dendritic (d) and cellular structures at mesolevel (e) and Al-Si composite at microlevel (f)

3.2 Formulation of the Mechanical Problem

The dynamic boundary-value problems on loading the layered structures and composites are solved in a three-dimensional formulation in the ABAQUS/Explicit solver. The printed layer and interlayer material in the layered structure at the macrolevel, the aluminum dendrites and the eutectic network in the dendritic structure and the remelted dendrites in the cellular structure of the interlayer at the mesolevel, and the aluminum matrix in the Al-Si composite are taken to be elastoplastic. Their mechanical response is described using the Hooke's law:

$$\dot{\sigma}_{ij} = -\dot{P}\delta_{ij} + \dot{S}_{ij} = K\dot{\varepsilon}_{kk}\delta_{ij} + 2\mu(\dot{\varepsilon}_{ij} - \dot{\varepsilon}_{kk}\delta_{ij}/3 - \dot{\varepsilon}_{ij}^{p}) \quad (1)$$

where σ_{ij} and S_{ij} are the stress tensor and stress deviator components, P is the pressure, ε_{ij} and ε_{ij}^{p} are the total and plastic strain components, δ_{ij} is the Kronecker delta, K and μ are the volumetric and shear moduli, the upper dot designates a time derivative.

The plastic flow is described using the plastic flow law $\dot{\varepsilon}_{ij}^{p} = \dot{\lambda} S_{ij}$ associated with the yielding condition given by $\sigma_{eq} - \varphi(\varepsilon_{eq}^{p}) = 0$, where λ is the scalar factor that is identically zero in the elastic region. The function of isotropic strain hardening of the materials represents a combination of the exponential and linear laws

$$\varphi\left(\varepsilon_{eq}^{p}\right) = \sigma_s - (\sigma_s - \sigma_0)\exp(-\varepsilon_{eq}^{p} / \varepsilon_r^{p}) \tag{2}$$

$$\varphi\left(\varepsilon_{eq}^{p}\right) = A + B\varepsilon_{eq}^{p}, \tag{3}$$

where σ_s and σ_0 are the ultimate stress and yield point, ε_r^{p} characterizes the strain hardening degree, A and B are the linear hardening constants, ε_{eq}^{p} and σ_{eq} are the stress and accumulated plastic strain intensities.

The response of silicon particle in the cellular structure of the interlayer at the mesolevel and in the eutectic Al-Si composite at the microlevel is elastic and is described by Eq. (1), where $\dot{\varepsilon}_{ij}^{p} = 0$.

The uniaxial compression in the scanning direction X is modeled by the kinematic boundary conditions for all the calculations performed in this study (Fig. 2). Particle velocities on the left and right surfaces were gradually increased to avoid dynamic effects. The top surface is free of loads, while the symmetry conditions are set on the bottom surface. Here, the elastic moduli at different spatial scales were determined from the mixture model. The eutectic modulus at the mesolevel and that of the layer at the macrolevel were calculated via the volume fractions of aluminum and silicon particles at the microlevel and via those of dendrites and eutectics at the mesolevel, respectively. The interlayer moduli at the macrolevel were calculated using the volume fraction of silicon particles and aluminum in the cellular structure at the mesolevel. For instance, for the modulus of volumetric compression we have

$$K_{Eut} = K_{Al} f + K_{Si}(1-f),\ K_{Layer} = K_{Al}\varphi + K_{Eut}(1-\varphi),\ K_{Interlayer} = K_{Al}\eta + K_{Si}(1-\eta), \tag{4}$$

where f, φ and η are the volume fractions of aluminum in the eutectics, aluminum dendrites in the layer, and aluminum in the interlayer, respectively.

4. Deriving Local Material Properties by Top-Down Analysis

In a microstructure-based numerical simulation, it is critically important to determine the local characteristics of the structure component materials at different spatial scales – their values could differ from the experimentally determined macroscopic properties by a few times due to the scaling factor. It is the main aim of the present study to determine the mechanical properties of materials in an additively manufactured Al-Si12 alloy. It is necessary to derive the properties of aluminum in dendrites and eutectics. In the course of a comparatively fast crystallization after its additive melting, aluminum formed in the

eutectic network between the submicron silicon particles can have a nanodefective structure. Its plasticity characteristics would be different from those in larger dendrites, where the dislocation mean free path is an order of magnitude larger. Unfortunately, it is impossible to determine the plastic properties of these materials necessary for the calculations, specifically the dependence of stresses on strains. Firstly, this is due to the fact that it is impossible to cut the samples of tens of microns, not to mention microns. Secondly, even given this possibility, there are no such testing machines to perform mechanical tensile or compressive tests of the samples as small as these. On the other hand, it is possible to carry out mechanical indentation testing, which would provide some indirect information on the local hardness and elasticity [29]. However, these data can be obtained from a limited scale – in our case at the mesolevel of the dendritic structure. It is impossible to do it at the microlevel, since in order to achieve a local area of indentation of tens of nanometers one needs a load of fractions of a millinewton. These indentations, though technically not improbable, lie beyond the testing machine resolution and are not correct.

Therefore, at the scales of microns and tens of microns the material properties are difficult or impossible to determine. In view of this fact, the use of combined numerical-experimental approaches is required, aimed at identifying the properties that would be further used in the calculations for the sake of identifying the features of deformation and fracture of additively manufactured alloys having a complex multiscale structure.

The top-down numerical-experimental approach proposed in this work consists in a derivation of the local properties of aluminum in the dendrites and, further, its properties in the eutectics. In so doing, we consistently use the macroscopic experiments on compression of the samples of an additively manufactured Al-Si12 alloy (Fig. 3a) and the nanoindetation data (Fig. 3b). The samples for mechanical tests were cut from the material along the scanning direction. The compressive tests were performed in a Testsystems machine (Testsystems, Russia). The loading rate was 1mm/min.

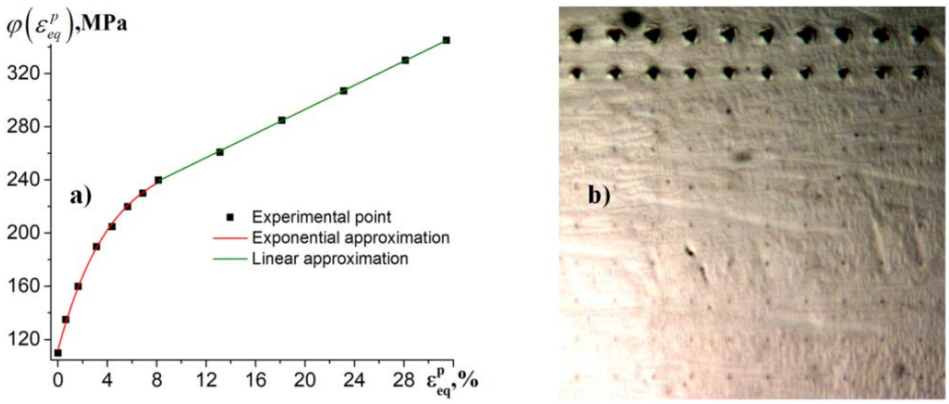

Fig. 3 Experimental response of macroscopic EBAM AlSi12 sample in compression along scanning direction X shown in Figs. 1 and 2 and its approximation by exponential and linear laws (a) and indentation points made by forces of 400, 100 and 10 mN (b)

4.1 Nanoindentation

In this work, we propose to estimate the inlayer, interlay, eutectic and aluminum material properties by the method of indentation. The hardness of the EBAM AlSi12 samples prepared for metallography was performed in a NanoTest machine (Micro Materials Ltd., Wrexham, UK) using a Berkovich diamond indenter under the applied load control mode. The maximum load was varied from 2 to 400 mN. At the loads of 200 and 400 mN, fifteen indents were made in every case, and at 2 and 10 mN – 100 indentations separated by a distance of 100 μm (Fig. 3b), which allowed ruling out the effect of plastic deformation on the measured characteristics. The loading and unloading durations were 20 s each. In order to correct the temperature drift after the 90% unloading, the samples were held at a constant load of 60 s. By analyzing the indentation curves using the Oliver-Pharr method we determined the sample hardness H and the reduced Young's modulus E*.

The indentations at a hold-down load of 400 mN demonstrate some of the integral characteristics of the dendritic material structure within the layer (Fig. 4a) and the cellular structure with the silicon particles surrounded by aluminum in the HAZ (Fig. 4b), since they cover a comparatively large area for averaging. Out of 15 indentations (10 are shown in Fig. 3b), only one fell within the interlayer (Fig. 4b); the images of the other 14 indentations in different sites of the layers are qualitatively similar to that given in Fig. 4a. It is from these 14 measurements that we determined the average material nanohardness – 0.71 GPa. Inside the interlayer, the material hardness is found to be 0.59 GPa. We can, therefore, take the layer-to-interlayer ratio of the mechanical properties of the materials to be 1.2. The curves of the load against the indentation area for all of the 15 indentations are qualitatively similar to those given in Fig. 4c, indicating that all measurements are correct.

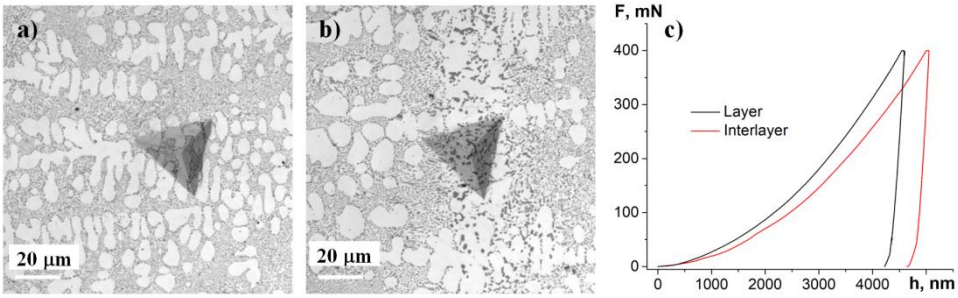

Fig. 4 Indenter imprints in printed layer (a) and in interlayer (b) and nanoindentation curves at a load of 400 mN (c)

The lower the indentation force, the stronger the influence of inhomogeneities on the measured results, therefore the less smoother and monotonic could be the indentation curves. On the other hand, in order to derive the mechanical properties of the micron structure elements, we need the smaller indentation imprints, which are formed at weaker loading forces. Therefore, for the sake of estimation of mechanical properties of aluminum in the dendrites and the eutectic material, we used the data measured at the least possible maximum force for this alloy of 2 mN, at which a sufficiently large percentage of correct measurement is available (Fig. 5). To begin with, from 100 measurements we removed 18 incorrect indentations identified by nonmonotonic curves (allowed monotonicity is shown

in Fig. 5c). Then two sets were compiled from the remaining measurements – the indentation traces falling within the center of either the dendrite (Fig. 5a) or the eutectics (Fig. 5b). The data in these two sets were averaged, and the hardness values of the eutectic and aluminum materials were determined, and so was their ratio – 1.7.

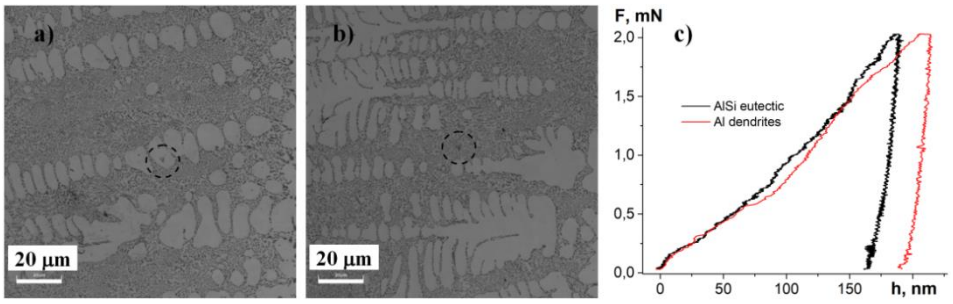

Fig. 5 Indenter imprints traces in dendrite (a) and eutectic network (b), indentation curves at a load of 2 mN (c)

4.2 Multiscale Top-Down Numerical Simulation

A top-down numerical analysis assumes a solution of boundary-value problems on deformation of structures at different spatial scales, starting from the macrolevel. At every spatial scale, an inverse problem is solved in order to select the constants of Eqs. (2) and (3) for the structure component materials.

At the macrolevel, we solved the problem of compression of a layered structure shown in Fig. 2a. The aim of the calculations was to select the plastic properties of the layer and interlayer materials to make sure that the calculated integral curve under the conditions of the layered structure compression would coincide with the experimental stress-strain curve given in Fig. 3a. In the initial iteration, the model parameters were determined from the mixture model using the results of nanoindentation at 400 mN (Fig. 4). It has been taken that the ratio of the layer and interlayer materials characterizes the difference in the flow stresses, σ_s and σ_0 in the exponential law and in the linear equation constants A and B. Based on the tilt of the indentation curves (Fig. 4c), we take that parameter ε_r^p is the same for the layer and interlayer materials. Since $H^{Layer} / H^{Interlayer}$ =1.2, at the macrolevel we obtain a system of equations:

$$\begin{aligned}
\sigma_0^{macro} &= \sigma_0^{Layer}\vartheta + \sigma_0^{Interlayer}(1-\vartheta);\ \sigma_0^{Layer} / \sigma_0^{Interlayer} = 1.2,\\
\sigma_s^{macro} &= \sigma_s^{Layer}\vartheta + \sigma_s^{Interlayer}(1-\vartheta);\ \sigma_s^{Layer} / \sigma_s^{Interlayer} = 1.2,\\
A^{macro} &= A^{Layer}\vartheta + A^{Interlayer}(1-\vartheta);\ A^{Layer} / A^{Interlayer} = 1.2,\\
B^{macro} &= B^{Layer}\vartheta + B^{Interlayer}(1-\vartheta);\ B^{Layer} / B^{Interlayer} = 1.2.
\end{aligned} \tag{5}$$

Denoting all 4 constants in Eq. (5) by the same symbol for the sake of convenience, we have

$$\xi^{macro} = \xi^{Layer}\vartheta + \xi^{Interlayer}(1-\vartheta);\ \xi^{Layer} / \xi^{Interlayer} = 1.2, \quad (6)$$

where ξ^{Layer} and $\xi^{Interlayer}$ are the derived properties of the layer and interlayer materials and ξ^{macro} are the known constants in the experimental flow curve approximation for the macrosample in compression (Fig. 3a). Since the volume fraction of the layer material is also known $\vartheta = 0.89$, from Eq. (6) we uniquely obtain the model layer and interlayer parameters that are further used as the first iteration in modeling the layered structure compression. This solution of the boundary-value problem at the macrolevel is a test solution, since in the case of a uniaxial compression along direction X, in which case the kinematic loading is effected along the layers and interlayers and the interlayer boundaries are presented by straight lines (Fig. 2a), the stress and strain distributions within the layers have to be homogeneous without any localization. Therefore, the integral calculation curve for this structure has to completely coincide with that obtained in accordance with the mixture model. This was the case in the calculations: the constants obtained using Eq. (6) did not require any iterative refinement; they provided a complete coincidence of the calculated and experimental curves (Table 1). The respective curves are shown in Fig. 6a. Here and further in the figures, the stress and strain in the calculated curves of structure deformation represents the stress and plastic strain intensities averaged over the computational domain.

Table 1 Plastic properties of the layer and interlayer materials determined from a numerical calculation of deformation of an AlSi12 layered sample at the macrolevel

	σ_s, MPa	σ_0, MPa	ε_r^p, %	A, MPa	B, MPa
Layer	266	114	4,2	210	430
Interlayer	219	94	4,2	170	360

Now let us turn to a lower scale level. The task in this stage is to determine plastic properties of the eutectic material and aluminum in the dendrites. We have to select the model parameters so as to let the calculated integral curve in the case of a dendritic structure compression at the mesolevel (Fig. 2d) coincide with the earlier obtained response of the layer material at the macrolevel, described by the derived constants ξ^{Layer}. At this level, we use the data of nanoindentation at 2 mN (Fig. 5), which characterize the difference in the mechanical properties of aluminum in the dendrites and the eutectic material by comparing their hardness values. Therefore, at the mesolevel Eq. (6) acquires the following form:

$$\xi^{Layer} = \xi^{Al}_{Meso}\chi + \xi^{Eutectic}(1-\chi);\ \xi^{Eutectic} / \xi^{Al}_{Meso} = 1.7, \quad (7)$$

where ξ^{Al}_{Meso} and $\xi^{Eutectic}$ are the derived properties of aluminum in the dendrites and the eutectic material. The volume fraction of aluminum dendrites is known $\chi = 0.42$, so using Eq. (7) we uniquely determine the model parameters as the first iteration. The aluminum dendrites inside the layer at the mesolevel have complicated shapes, there are stress concentrations and strain localization near the curvilinear interfaces between the eutectics and the dendrites. Therefore, the constants ξ^{Al}_{Meso} and $\xi^{Eutectic}$ determined from the mixture model fail to provide an agreement between the calculated integral flow curve of the dendritic structure and the stress-strain curve of the layer derived at the macrolevel. In this case, it is necessary to derive these parameters via their successive variation when solving the direct

boundary-value problems on the dendritic structure compression. The resulting parameters are listed in Table 2, and the respective curves obtained at the mesolevel – in Fig. 6b.

Table 2 Plastic properties of AlSi eutectics and Al dendrites determined from numerically calculated dendritic structure deformation at mesolevel

	σ_s, MPa	σ_0, MPa	ε_r^p, %	A, MPa	B, MPa
AlSi eutectic	337	143	4,4	270	500
Al in dendrites	198	84	4,4	160	290

To sum up, in this step of the top-down numerical-experimental analysis we have determined the plastic material properties at the mesolevel, specifically we have derived the stress-strain curves of the eutectics and dendrites, which are impossible to obtain experimentally. In addition, at this level of consideration it is also possible to estimate the local mechanical properties using nanoindentation, which was successfully done.

At the microlevel, a still lower spatial scale, it is hardly possible to experimentally estimate the local material properties by nanoindentation. The results that allow deriving the material properties at the submicron level through numerical simulations are therefore ever more valuable. Similarly, if we follow the above-described procedure, an etalon curve for deriving the properties of aluminum surrounding silicon particles measuring hundreds of nanometers (Fig. 1d–f) is the flow curve for the eutectics material obtained at the mesolevel and determined by the constants $\xi^{Eutectic}$ (Table 2). No additional conditions based on the indentation data are required at the microlevel, since silicon particles are not subjected to plastic deformation, and the elastic moduli are known and are taken to be independent of the spatial scale in the range up to 100 nm. In view of these considerations, at the microlevel we solved an inverse problem of selection of the model parameters for aluminum in eutectics ξ_{Micro}^{Al} via performing a series of numerical experiments on compression of a structure given in Fig. 2f. The derived mechanical properties of aluminum at the submicron level are presented in Table 3. The flow curve calculated for the Al-Si composite and the derived aluminum properties are given in Fig. 6c.

Table 3 Plastic properties of aluminum in eutectics, determined from numerical calculation of deformation of Al-Si composite at microlevel

Material	σ_s, MPa	σ_0, MPa	ε_r^p, %	A, MPa	B, MPa
Al in Eutectic	315	133	8,5	260	180

It was a priori assumed that at the mesolevel aluminum in dendrites inside the layer and in the cellular structure in the interlayer has the same defect structure, i.e. it is the same material with the same mechanical properties. Therefore, one could derive them without modeling the dendritic structure deformation, as it was mentioned above (Path 1), but determine the constants, ξ_{Meso}^{Al} and $\xi^{Eutectic}$, via solving the problem on deformation of a cellular structure shown in Fig. 2e to achieve a consistency between the calculated integral curve and the interlayer material properties derived at the macrolevel and characterized by its constants $\xi^{Interlayer}$ (Path 2). Let us verify this assumption by calculating the cellular structure deformation using the aluminum properties already determined at the mesolevel

via Path 1 ξ_{Meso}^{Al}, which are highlighted in Fig. 6b by a cyan curve with stars. The respective calculation results are presented in Fig. 6d. It is seen that the calculated flow curve (orange with triangles) perfectly coincides with the mechanical interlayer properties, determined at the macrolevel under compression of the structure to 8 %, and starts deflecting upwards at larger strains. This implies that the properties of aluminum in the interlayer and in the dendrites under intensive straining might differ. The reason for the differences could stem from the differences in the aluminum properties in the cell walls and inside the cells, since in the former the dislocation mean free path between the closely located silicon particles is small, which provides a better strain hardening effect.

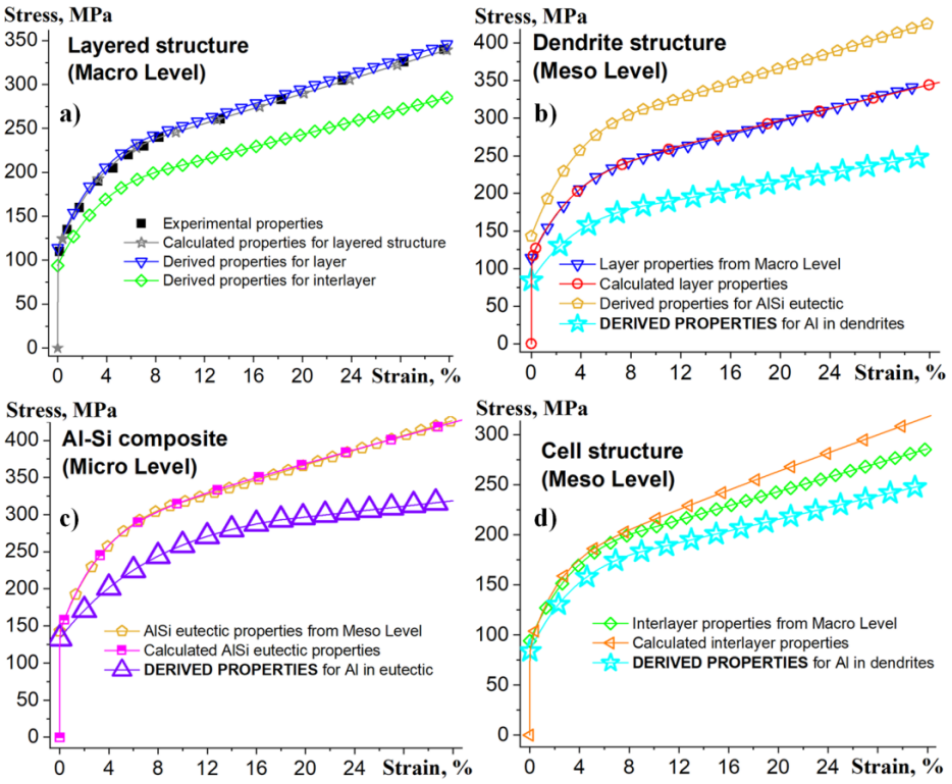

Fig. 6 Stress-strain curves of structure elements of additively manufactured Al-Si12 alloy at macro- (a), meso- (b, d) and microscales (c)

Figs. 7 and 8 illustrate an inhomogeneous stress-strain state at the mesolevel. It is seen that a complex stressed state is formed in the dendritic structure (Fig. 7a). In the eutectics, the level of stress intensity is higher than that in the dendrites. Both the eutectics and the dendrites are prevailingly found in the state of volumetric compression (Fig. 7b). In the vicinity of the upper free surface above two elongated dendrites, there are two local volumetric tension regions formed due to bending of the eutectic framework. It is evident from Fig. 7b that the regions of approximately the same highly compressive pressure are

formed both in minor-, average-size dendrites, and eutectic network between the dendrites located on top of each other. It is noteworthy that the stress intensity in the dendrites is much lower than that in the network. This suggests that the eutectic network undergoes larger shear loading that do the dendrites. Moreover, the pressure between the adjacent intergrown dendrites is low, and in some regions is close to zero (blue and green areas in Fig. 7b), considering that the stress intensity is at its maximum (Fig. 7a). This indicates that the eutectic network material is in the state close to pure shear. The stresses in the eutectics and dendrites concentrate due to the plastic flow localization; therefore, the distributions in Fig. 7a and c are qualitatively similar. It is worth noting that even at a 32 % compression there are regions in the eutectic network, wherein the plastic deformation is on the order of 2–5% (blue areas in Fig. 7c). The stress intensity in these regions is low (Fig. 7a), while the pressure is quite high (Fig. 7b), implying that they undergo merely pure volumetric compression.

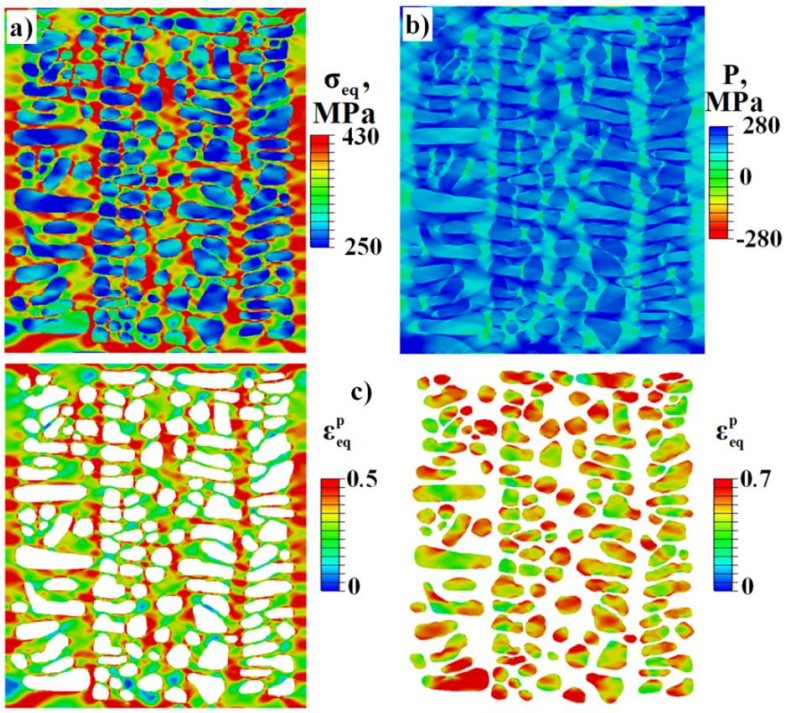

Fig. 7 Compression of dendritic structure shown in Fig. 2d to 32 %. Stress intensity (a) and pressure patterns (b). Accumulated plastic strain patterns presented separately for the eutectic network and dendrites (c). Undeformed shape

A different pattern is observed in the case of the cellular structure deformation in the interlayer (Fig. 8). A distinguishing feature is the fact that, considering the overall compression, both the aluminum matrix and the silicon particles contain regions of volumetric tension (red areas in Fig. 8a). In the matrix, these regions are found near the particle convexities in the direction perpendicular to that of compression, while in the

particles near the matrix–particle interface concavities along the direction of compression. The values of both the negative pressure (Fig. 8a) and the stress intensity are comparable and large, implying that these are the regions of a high-intensity volumetric-shear straining. Between the regions of volumetric tension and compression, i.e. where the pressure changes its sign (green area sin Fig. 8a), the stress intensity is, though not the highest, but quite high, measuring hundreds of megapascals. Therefore, the conditions of moderate pure shear are realized there. The maximum compressive and tensile stresses develop in the intricately-shaped particles with curvilinear interfaces with the matrix (Fig. 8a). The highest plastic strain localization is observed in the cell walls between the closely spaced silicon particles, while inside most cells the localization is not so pronounced (Fig. 8c). Due to a complex morphological anisotropy of this structure, however, the stresses might concentrate in the centers of individual cells and there might develop a stress concentration resulting in a developed plastic flow (dashed circle in Fig. 8c). In the matrix of the cellular structure there are also weakly deformed regions (blue areas in Fig. 8c). These regions are more numerous, and the plastic strain intensity in them is an order lower than that in the dendritic structure (cf. Figs. 7c and 8c). In fact, these are the regions of nearly elastic deformation that might be found in the conditions of shear or volumetric compression, or their combination (cf. Fig. 8a–c). The elastic regions are located both near the concavities

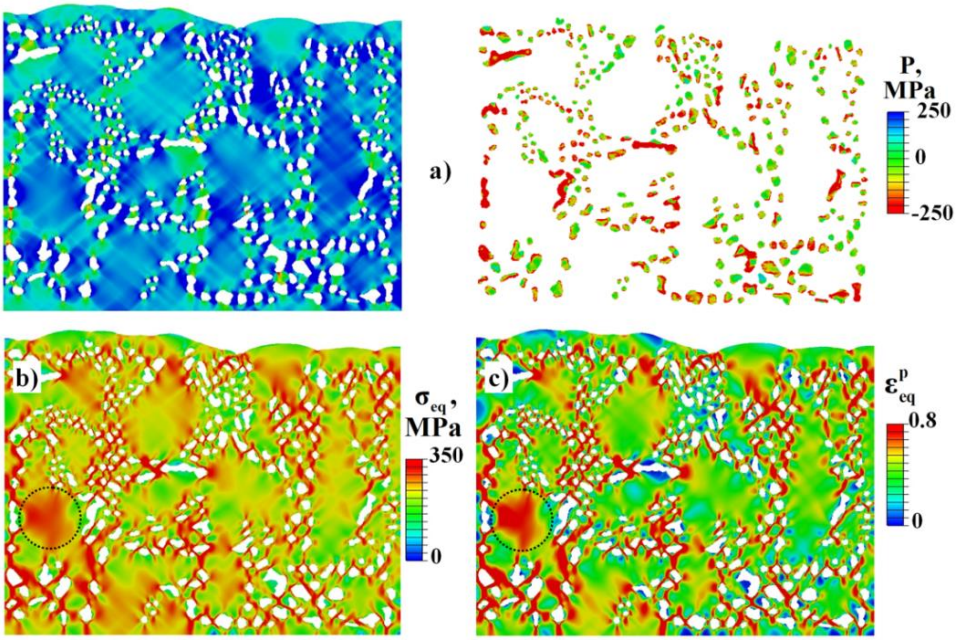

Fig. 8 Compression of interlayer structure shown in Fig. 2e to 32%. Pressure distributions presented separately for the aluminum matrix and silicon particles (a), stress intensity (b) and accumulated plastic strain patterns in the aluminum matrix (c). Deformed shape

between the elongated particles and the matrix, and between the closely spaced silicon particles. At the microlevel, the same qualitative behavior patterns are observed in the

composite material of the eutectics as in the cell walls, since it represents the same *aluminum matrix–silicon particles* composite material. From the quantitative point, the difference consists in the following: firstly, the average stresses at the microlevel are higher than at the mesolevel, since aluminum in the eutectics possesses higher mechanical properties than aluminum in the dendrites. Secondly, above-described peculiarities of formation of the volumetric compression and tension regions, as well as the weakly deformed regions, are not so strongly pronounced, since the submicron silicon particles have less complicated shapes than those of large silicon particles in the interlayer.

5. CONCLUSIONS

Using an AlSi12 alloy fabricated by a wire-feed electron-beam additive manufacturing, a top-down approach to a numerical-experimental derivation of local mechanical properties of hierarchically organized composite materials has been proposed. The structure of this WEBAM AlSi12 alloy has been examined by the methods of optical, scanning and transmission electron microscopy at different spatial scale levels. The experiments on compression and nanoindentation of the WEBAM AlSi12 alloy samples have been performed. Using the experimentally obtained images, a number of finite-element models were generated of the layered structure at the macrolevel, of the dendritic and composite cellular structure at the mesolevel, and of the aluminum matrix–silicon particles composite structure – at the microlevel. These models were integrated into the ABAQUS/Explicit solver and the respective boundary-value problems were solved. The principle of the proposed top-down analysis consists in a successive series of numerical calculations of compression of the structures at different spatial scale, starting from the macro scale. An inverse problem of derivation of the mechanical properties of aluminum in the dendrites of about tens of microns and aluminum in the eutectic material at the submicron scale was solved. To begin with, we solved the problem of the layered structure compression. The macroscopic flow curve and the data of large indentation loads were used to derive the material properties inside the printed layer and in the interlayer. These properties and the indentation data at small loads were then used at the mesolevel to derive the properties of aluminum dendrites and eutectic network in modeling the dendritic structure compression. Finally, using the obtained eutectic properties, we solved the problems on compression of the particle-reinforced Al-Si composite at the microlevel and derived the plastic properties of aluminum surrounding silicon particles measuring hundreds of nanometers.

An analysis of the inhomogeneous stressed state of the structures of different spatial scales under the conditions of their compression has prompted the following conclusions:

– in the case of compression of the dendritic structure inside the layer, the eutectic network is more prone to shear stresses than the dendrites, and the regions between the neighboring dendrites experience a state close to pure shear;

– in the case of 30 % deformation, there are weakly deformed regions in the eutectic network, which undergo a state close to a purely volumetric compression, implying that the plastic deformation is small; it is found to be about 3 %;

– in the case of compression of the cellular structure observed in the interlayer, both in the aluminum matrix and in the silicon particles there are regions of high-intensity volumetric tension and shear and the regions of pure shear. The largest compressive and

tensile stresses develop in large particles of complicated shapes having curvilinear interfaces with the matrix;

– maximum plastic strain localization is found in the cell walls between the closely located silicon particles, and inside most of the cells it is less clearly pronounced;

– there are a larger number of weakly deformed regions in the cellular structure than in the dendritic structure; minimum plastic strain is found to be 0.2 %.

Acknowledgement: *The work was supported by the Russian Science Foundation (grant No. 23-11-00222, https://rscf.ru/en/project/23-11-00222/). Basic user-defined subroutine for calculating plasticity in ABAQUS/Explicit (№ 2022682210/08.11.22) was developed according to the Government research assignment for ISPMS SB RAS, project FWRW-2021-0002.*

REFERENCES

1. Elmasry, A., Azoti, W., El-Safty, S.A., Elmarakbi, A., 2023, *A comparative review of multiscale models for effective properties of nano- and micro-composites*, Progress in Materials Science, 132, 101022.
2. Zhu, Y., He, C., Zhao, T., Li, Y., 2024, *Towards accurate prediction of the dynamic behavior and failure mechanisms of three-dimensional braided composites: A multiscale analysis scheme*, Thin-Walled Structures, 203, 112188.
3. Li, M., Li, S., Tian, Y., Zhang, H., Zhu, W., Ke, Y., 2024, *Bottom-up stochastic multiscale model for the mechanical behavior of multidirectional composite laminates with microvoids*, Composites Part A: Applied Science and Manufacturing, 181, 108144.
4. Yao, H., Bai, T., He, X., Wang, Q., Gu, S., Shi, S.Q., Yan, J., Lu, J., Wang, D., Han, G., Cheng, W., 2024, A novel multiscale prediction strategy for simulating the progressive damage behavior of plain-woven bamboo fabrics reinforced epoxy resin composites, Composites Science and Technology, 253, 110662.
5. Więckowski, J., Sałabun, W., 2025, *Comparative Sensitivity Analysis in Composite Material Selection: Evaluating OAT and COMSAM Methods in Multi-criteria Decision-making*, Spectrum of Mechanical Engineering and Operational Research, 2(1), pp. 1-12.
6. Sames, W.J., List, F.A., Pannala, S., Dehoff, R.R., Babu, S.S., 2016, *The metallurgy and processing science of metal additive manufacturing*, International Materials Reviews, 61(5), pp. 1-46.
7. Leung, C.L.A., Tosi, R., Muzangaza, E., Nonni, S., Withers, P.D., Lee, P.D., 2019, *Effect of preheating on the thermal, microstructural and mechanical properties of selective electron beam melted Ti-6Al-4V components*, Materials & Design, 174, 107792.
8. Griffiths, S., Ghasemi Tabasi, H., Ivas, T., Maeder, X., De Luca, A., Zweiacker, K., Wróbel, R., Jhabvala, J., Logé, R.E., Leinenbach, C., 2020, *Combining alloy and process modification for micro-crack mitigation in an additively manufactured Ni-base superalloy*, Additive Manufacturing, 36, 101443.
9. Shete, H., Chavan, V., 2023, *Development of fuel filter cap of comet diesel engine using structural optimization technique and additive manufacturing*, Engineering Review, 43(2), pp. 48-56.
10. Baek, G.Y., Shin, G.Y., Lee, K.Y., Shim, D.S., 2019, *Mechanical properties of tool steels with high wear resistance via directed energy deposition*, Metals, 9(3), 282.
11. Zhang, M., Zhou, X., Wang, D., He, L., Ye, X., Zhang, W., 2022, *Additive manufacturing of in-situ strengthened dual-phase AlCoCuFeNi high-entropy alloy by selective electron beam melting*, Journal of Alloys and Compounds, 893, 162259.
12. Geng, Y., Panchenko, I., Konovalov, S., Chen, X., Ivanov, Y., 2021, *Effect of electron beam energy densities on the surface morphology and tensile property of additively manufactured Al-Mg alloy*, Nuclear Instruments and Methods in Physics Research Section B: Beam Interactions with Materials and Atoms, 498, pp. 15-22.
13. Davis, A.E., Kennedy, J.R., Strong, D., Kovalchuk, D., Porter, S., Prangnell, P.B., 2021, *Tailoring equiaxed β-grain structures in Ti-6Al-4V coaxial electron beam wire additive manufacturing*, Materialia, 20, 101202.
14. Kalashnikov, K.N., Chumaevskii, A.V., Kalashnikova, T.A., Kolubaev, E.A., 2022, *A substrate material and thickness influence on the 3D-printing of Ti–6Al–4V components via wire-feed electron beam additive manufacturing*, Journal of Materials Research and Technology, 16(5), pp. 840-852.
15. Pixner, F., Buzolin, R., Warchomicka, F., Pilz, A., Enzinger, N., 2022, *Wire-based electron beam additive manufacturing of tungsten*, International Journal of Refractory Metals and Hard Materials, 108, 105917.

16. Pu, Z., Du, D., Wang, K., Liu, G., Zhang, D., Liang, Z., Xi, R., Wang, X., Chang, B., 2022, *Evolution of transformation behavior and tensile functional properties with process parameters for electron beam wire-feed additive manufactured NiTi shape memory alloys*, Materials Science and Engineering: A, 840, 142977.
17. Ahammed, D.S., Razin, A.A., Khan, A.A., Kaiser, M.S., 2024, *Mechanical properties of hypoeutectic, eutectic, and hypereutectic Al-Si automotive alloys under ageing treatment*, Engineering Review, 44(1), pp. 1-13.
18. Zhu, Z., Hu, Z., Li Seet, H., Liu, T., Liao, W., Ramamurty, U., Mui Ling Nai, S., 2023, *Recent progress on the additive manufacturing of aluminum alloys and aluminum matrix composites: Microstructure, properties, and applications*, International Journal of Machine Tools and Manufacture, 190, 104047.
19. Knapp, G.L., Gussev, M., Shyam, A., Feldhausen, T., Plotkowski, A., 2022, *Microstructure, deformation and fracture mechanisms in Al-4043 alloy produced by laser hot-wire additive manufacturing*, Additive Manufacturing, 59A, 103150.
20. Fan, Y., Chen, F., Cao, S., Hu, Y., Xie, R., Yang, Y., 2023, *Effect of interlayer coating La_2O_3 particles on arc behavior and microstructure of wire arc additive manufacturing Al-Si alloy deposition*, Journal of Manufacturing Processes, 101, pp. 943-958.
21. Wu, X., Meng, Y., Ye, Y., Jiang, Y., Zhang, B., Chen, H., 2024, *Improved formation accuracy and mechanical properties of laser-arc hybrid additive manufactured aluminum alloy through beam oscillation*, Optics & Laser Technology, 170, 110325.
22. Shi, Y., Gong, S., Xu, H., Yang, G., Qiao, J., Wang, Z., Zhang, J., Qi, B., 2023, *Electron beam metal additive manufacturing: Defects formation and in-process control*, Journal of Manufacturing Processes, 101, pp. 386-431.
23. Huang, W., Chen, S., Xiao, J., Jiang, X., Jia, Y., 2021, *Laser wirefeed metal additive manufacturing of the Al alloy*, Optics & Laser Technology, 134, 106627.
24. Kolubaev, E., Rubtsov, V., Chumaevskii, A., Astafurova, E., 2022, *Micro-, Meso- and Macrostructural Design of Bulk Metallic and Polymetallic Materials by Wire-Feed Electron-Beam Additive Manufacturing*, Physical Mesomechanics, 25, pp. 479-491.
25. Balokhonov, R., Zemlianov, A., Gatiyatullina, D., Romanova, V., 2025, *Numerical Study of Residual Stress Effects on Deformation and Fracture in Metal Matrix Composites*, Spectrum of Mechanical Engineering and Operational Research, 2(1), pp. 219-230.
26. Zemlyanov, A.V., Gatiyatullina, D.D., Utyaganova, V.R., Dymnich, E., Shamarin, N.N., Nikonov, S.Y., Romanova, V.A., Kulkov, A.S., Balokhonov, R.R., 2023, *A Study of Deformation and Fracture of the Eutectic in an Additively Manufactured Al-Si Composite Alloy*, Physical Mesomechanics, 26(5), pp. 678-690.
27. Balokhonov, R., Zemlianov, A., Utyaganova, V., Gatiyatullina, D., Romanova, V., 2023, *Two-Scale Computational Analysis of Deformation and Fracture in an Al-Si Composite Material Fabricated by Electron Beam Wire-Feed Additive Manufacturing*, Metals, 13(9), 1465.
28. Balokhonov, R., Utyaganova, V., Gatiyatullina, D., Zemlianov, A., Romanova, V., 2024, *Interlayer effect on deformation and fracture of dendritic structure formed during wire-feed electron-beam additive manufacturing of Al-Si alloy*, Facta Universitatis. Series: Mechanical Engineering, 22(3), pp. 515-527.
29. Petruš, P., Barényi I., Majerík J., 2023, *Microstructure investigation of cast irons with nodular and flake graphite via nanoindentation*, Engineering Review, 43(2), pp. 1-7.